



1

2 **Near Global Distributions of Overshooting Tops Derived from Terra and Aqua MODIS**
3 **Observations**

4 Yulan Hong, Robert J. Trapp, Stephen W. Nesbitt and Larry Di Girolamo

5

6 Department of Atmospheric Sciences, University of Illinois Urbana-Champaign, Urbana,
7 Illinois, USA

8 Corresponding author: Yulan Hong

9 Email: yulanh@illinois.edu

10

11 **Abstract**

12 Overshooting cloud tops (OT) form in deep convective storms when strong updrafts overshoot
13 the tropopause. An OT is a well-known indicator for convective updrafts and severe weather
14 conditions. Here, we develop an OT detection algorithm using thermal IR channels and apply
15 this algorithm to about 20-year MODIS data from both Terra and Aqua satellites to form an
16 extensive, near global climatology of OT occurrences. The algorithm is based on a logistic model
17 which is trained using A-Train observations. We demonstrate that the overall accuracy of our
18 approach is about 0.9 when the probability of the OT candidates is larger than 0.9. The OT
19 climatology reveals a pattern that follows the climatology of deep convection, as well as shallow
20 convection over the mid-latitude oceans during winter cold air outbreaks. OTs appear most
21 frequently over the Intertropical Convergence Zone (ITCZ), central and southeast North
22 America, tropical and subtropical South America, southeast and south Asia, tropical and
23 subtropical Africa, and northern middle-high latitudes. OT spatial distributions show strong
24 seasonal and diurnal variabilities. Seasonal OT variations shift with large-scale climate systems
25 such as the ITCZ and local monsoonal systems, including the South Asian Monsoon, North
26 American Monsoon and West African Monsoon. OT diurnal variations agree with the known
27 diurnal cycle of convection: Maximum OT occurrences are in the afternoon over most land area
28 and around midnight over ocean; and the OT diurnal cycle is stronger and more varied over land
29 than over ocean. OTs over land are usually colder than over ocean except around 10:30 am. The
30 top 10 coldest OTs from both Terra and Aqua mostly occur over land and at night. This study
31 provides OT climatology for the first time derived from two-decade MODIS data that represents
32 the longest and stable satellite records.

33

34

35

36

37

38



39

40 1. Introduction

41 An overshooting cloud top (OT) forms when a convective-storm updraft penetrates the
42 level of neutral buoyancy and thus extends into the upper troposphere-lower stratosphere
43 (UTLS). OTs and their associated strong updrafts have been found to be an important transport
44 mechanism for water vapor and other atmospheric constituents into the stratosphere, thus
45 impacting the chemical composition and radiation budget of the UTLS (e.g. Gettelman et al.,
46 2002, 2004). They are often used as indicators of hazardous weather conditions such as strong
47 winds, large hail, flooding, and tornadoes at the Earth's surface (Bedka et al., 2018; Dworak et
48 al., 2012; Marion et al., 2019). More generally, the characteristics of OTs express information
49 about the characteristics of the related updrafts well below cloud top, including the convective
50 mass flux through the troposphere, which is an important parameterized quantity used in global
51 climate models.

52 In addition to the expectation of a connection between updraft strength and OT depth
53 (Heymsfield et al., 2010), Trapp et al. (2017) has shown a strong link between updraft core area
54 and OT area (OTA), indicating that a relatively intense and wide mid-tropospheric updraft core
55 area will tend to have a large OTA. Given that the direct measurements of updrafts within
56 intense convective environments are either from a few ground-based radars or several field
57 campaigns, these studies suggest a pathway for characterizing global updraft and updraft-size
58 distributions by quantifying the global OT distributions and characteristics from space.

59 Toward this end, the first step is to detect OTs. Geostationary satellite imagery provides
60 the opportunity to study OT occurrence over a wide region with fine spatial and temporal
61 resolutions. A series of OT detection algorithms have been developed based on geostationary
62 satellite observations. A commonly used OT detection method utilizes the brightness temperature
63 (T_b) difference (BTD) between Infrared (IR) water vapor (WV) and IR window channels (IRW)
64 (Schmetz et al., 1997). The WV-IRW BTD method is based on the fact that water vapor
65 transported into the lower stratosphere absorbs and emits more radiation at a water vapor channel
66 (such as $6.7\mu\text{m}$) compared to a window channel (such as $11\mu\text{m}$). Thus, positive BTD is usually
67 observed in the OT regions. However, in convective anvils (e.g. Hong & Di Girolamo, 2020;
68 Setvák et al., 2013) or in polar winter conditions when strong radiation inversions exist near the
69 surface (Ackerman, 1996), positive BTDs are also observed, which pose challenges to
70 differentiate OTs from these cases.

71 Another commonly used OT detection method is the IR Window (IRW) texture approach
72 (Bedka et al., 2010). This method uses a threshold of 215 K T_b at IR window channel to first
73 select OT candidates. These candidates are also colder than the tropopause temperatures. In the
74 second step, surrounding anvil is sampled at a ~ 8 km radius in 16 directions. At each direction,
75 pixels with T_{b11} colder than 225 K are included in calculating cirrus mean T_{b11} . The selected
76 candidate is considered as an OT if the T_{b11} difference between the pixel and its surrounding
77 cirrus is larger than a threshold of 6.5 K. The IRW texture approach has been widely applied for
78 OT detections observed from space such as geostationary satellite imagery and Moderate
79 Resolution Imaging Spectroradiometer (MODIS) (Bedka, 2011; Dworak et al., 2012; Griffin,
80 2017; Griffin et al., 2016; Monette et al., 2012; Proud, 2015). However, the strictly fixed
81 thresholds of IRW texture method limit its ability to detect warm OTs that commonly occur in



82 the mid-latitude regions, leading to seasonal and regional biases (Bedka & Khlopenkov, 2016).
83 Based on the visible (VIS) and IR imagery, Bedka and Khlopenkov (2016) developed a new
84 probabilistic OT detection algorithm to minimize the dependence of IRW texture method on
85 thresholds. Khlopenkov et al. (2021) further updated this algorithm by incorporating the
86 normalized tropopause temperature, surrounding anvil area and spatial uniformity. Improved
87 accuracy is achieved with this probabilistic OT detection algorithm compared to the IRW texture
88 method.

89 Observations from spaceborne active sensors have also been used for exploring OT
90 detections. For instance, the cloud profiling radar (CPR) on CloudSat (Stephens et al., 2008) was
91 used for validating the passive satellite-based OT detection methods (Bedka et al., 2010; Dworak
92 et al., 2012; Rysman et al., 2017), calculating the heights of OTs (Griffin et al., 2016), and
93 understanding WV-IRW BTD variability in OT regions (Setvák et al., 2013). The combined
94 CloudSat-CALIPSO (Cloud-Aerosol Lidar and Infrared Pathfinder Satellite Observation) data
95 was also used for detecting OTs, which led to the creation of a 12-year OT database (Li et al.,
96 2022). As demonstrated by these studies, the CloudSat-CALIPSO observations are powerful in
97 detecting OTs and gauging OT depths, but they are only available in a narrow swath that leads to
98 a lack of knowledge of three-dimensional (3-D) OT structures and large uncertainties in their
99 coverage (Astin et al., 2001). The precipitation radar on Tropical Rainfall Measuring Mission
100 (TRMM) or Global Precipitation Mission (GPM) can provide 3-D depictions of storm structures.
101 The precipitation radar observations have been used to investigate OT climatology including
102 their geodistributions, area and diurnal cycles in the tropical regions (20°S – 20°N) (Alcala &
103 Dessler, 2002; Liu & Zipser, 2005) and over broader areas (60°S – 60°N) (Hourngir et al., 2021;
104 Liu et al., 2020; Liu & Liu, 2016).

105 In addition, using three water vapor channels of the Advanced Microwave Sounding Unit
106 B (AMSU-B), convective overshooting detection method was developed through the microwave
107 technique (Hong et al., 2005). A seven-year OT climatology based on AMSU-B was derived in
108 the tropical and subtropical areas that shows OT interannual to diurnal variations (Hong et al.,
109 2008).

110 While many OT detection algorithms have been developed either using passive or active
111 remote sensing techniques, their use toward quantifying OT occurrences and attributes from
112 space are mostly from datasets with large spatial resolutions, e.g. ≥ 2 km for geostationary
113 satellites, 4-5 km for TRMM precipitation radar, 5 km for GPM Ku radar, and 15 km for AMSU-
114 B. Spatial resolution of observations significantly influences variations of WV-IRW BTD
115 (Setvák et al., 2007) and thus influences the choice of T_b and BTD thresholds. Large spatial
116 resolution also poses challenge in identifying OTs of small size and affects the accuracy of
117 computing OT attributes such as OT area. Therefore, measurements from space with a higher
118 spatial resolution will support a better characterization of OT climatology globally, which has
119 not been derived so far.

120 The MODIS instrument (King et al., 1992) acquires data at a high spatial resolution (≤ 1
121 km) that allows to detect small OTs. This sensor has a wide view swath of 2330 km which is able
122 to take a whole picture of a mesoscale system. It is operating on both Terra and Aqua satellites,
123 overpassing the same latitude at four different times each day: around 1:30am/pm and
124 10:30am/pm equator-crossing time (ECT). In the last twenty years, both Aqua and Terra



125 satellites have a consistent equator-crossing time, making the MODIS data the longest stable
126 climate records from space.

127 To utilize these climate records, the main objective of this study is to show a near global
128 climatology of OT occurrence derived from about 20-yr Aqua and Terra MODIS data. Owing to
129 the relatively high spatial resolution of MODIS, this climatology includes OTs in small size that
130 missed by GPM radar. It includes both the tropical and mid-latitude regions, and thus makes
131 complementary to the climatology by Liu & Zipser (2005) and Hong et al., (2008) that were
132 only focused on tropical and subtropical regions. It also provides OT diurnal information at four
133 observation times. To achieve these objectives, we first develop an OT detection algorithm that
134 is specifically designed for MODIS, works for both day and nighttime, and is more flexible to
135 thresholds compared to those used in Bedka et al. (2010) and Li et al. (2022). In sect. 2, we will
136 present the details of data and methods used for developing the OT detection algorithm.
137 Validation of the algorithm will be discussed in Sect. 3. Section 4 discusses the results produced
138 from our OT detection algorithm. Finally, in sect. 5, we conclude the findings of this study.

139 2. Data and Methodology

140 In order to develop a method that can detect OTs during both daytime and nighttime, this
141 study uses observations from multiple sensors onboard multiple platforms as well as a machine
142 learning method – logistic regression. The OT detection algorithm is developed in two main
143 steps. First, we manually identified a number of OT candidates from the combined CloudSat-
144 CALIPSO data. The infrared radiative characteristics of these OTs extracted from the combined
145 Aqua MODIS infrared data serve as inputs to train the logistic regression. Second, we applied
146 the regressed model to the Terra and Aqua MODIS data for automatic OT detection. We call this
147 method an *IR algorithm*.

148 2.1 Satellite and Reanalysis Datasets

149 2.1.1 CloudSat and CALIPSO

150 The CloudSat and CALIPSO satellites are two members of the afternoon constellation in
151 a sun-synchronous orbit with an Equator-crossing time at 01:30/13:30 local time (LT). The cloud
152 profiling radar (CPR) onboard CloudSat is a near-nadir-view radar operated at 94 GHz (~ 3.3
153 mm). Measuring radar reflectivity factor, the CPR probes the vertical structure of hydrometeors
154 with a minimum sensitivity of about -30 dBZ (Stephens et al., 2002, 2008). The radar's footprint
155 is 1.8 km along track and 1.4 km cross track. Its vertical resolution is 480 m with a resampled
156 resolution of 240 m. The radar is able to penetrate thick clouds and therefore is suitable for OT
157 identification as demonstrated by previous studies (Chung et al., 2008; Rysman et al., 2017;
158 Setvák et al., 2013). The radar reflectivity factor from the 2B-GEOPROF (Version P1) product
159 (Marchand et al., 2008) that shows time-height cross sections (curtains) of clouds and
160 precipitation was used for manual OT identification.

161 The CALIPSO flew about 15 s after CloudSat during the time period of observations
162 used in this work. The lidar onboard CALIPSO operates at 532 nm, having a vertical resolution
163 of 30 m below 8.2 km and 60 m above 8.2 km (Winker et al., 2003). The lidar is sensitive to
164 optically thin clouds and aerosols. The 2B-CLDCLASS-LIDAR product, provided by the
165 CloudSat Data Processing Center, reports cloud top and base heights for up to five layers (Wang
166 et al., 2012). This product utilizes the complementary features of the CloudSat radar and the



167 CALIPSO lidar, and thus includes thin cirrus clouds. The cloud top height of the topmost layer
168 was used to aid identifying OTs. Two years of 2B-GEOPROF and 2B-CLDCLASS-LIDAR data
169 (2007-2008) were used in this study.

170 **2.1.2 MODIS**

171 MODIS onboard both the Aqua and Terra platforms has 36 discrete spectral bands
172 between 0.415 to 14.235 μm with spectral-dependent spatial resolutions varying between 250 m
173 to 1 km at nadir (Barnes et al., 1998; King et al., 1992). The Aqua satellite launched in May 2002
174 is a member of A-Train satellite constellation. Terra was launched in December 1999 in a sun-
175 synchronous orbit with an Equator-crossing time at 10:30/22:30 LT (Platnick et al., 2003).

176 To obtain OT radiative characteristics, the MODIS Collection 6.1 Level 1B calibrated
177 radiance data, MYD021KM from Aqua and MOD021KM from Terra, were used. In this study,
178 the bands selected have center wavelength at 6.715 and 11.03 μm for OT detection that are used
179 for deriving brightness temperature. The uncertainties associated with these two bands are within
180 1% for both Terra and Aqua MODIS (Xiong et al., 2005, 2018). Navigation files with 1 km
181 resolution (MYD03 and MOD03) were used for the geolocation information. The Aqua MODIS
182 data from 2007-2008 were collocated to the CloudSat-CALIPSO data for selecting OT cases as a
183 training dataset for the logistic regression model (Sect. 2.2). The Terra MODIS data from
184 February 2000 – 2021 and the Aqua MODIS data from July 2002 -2021 were used for deriving
185 the OT climatology presented in Section 4.

186 **2.1.3 GPM**

187 The Global Precipitation Monitor (GPM) core observatory, launched in February 2014,
188 carries the first space-borne Dual-frequency Precipitation Radar (DPR) that includes a Ka-band
189 (35.5 GHz) radar (KaPR) and a Ku-band (13.6 GHz) radar (KuPR) (Hou et al., 2014). The KuPR
190 measures 3-D structures of convective systems with a vertical resolution of 250 m and a footprint
191 of 5 km over a swath of 245 km. The GPM KuPR echoes have been demonstrated to be effective
192 in the study of deep convection reaching to tropopause (Liu et al., 2020; Liu & Liu, 2016). To
193 utilize the GPM as an independent detection of OTs, we collocated the Ku-band echoes to the
194 OT candidates identified from Terra MODIS as a validation of our IR algorithm (Sect. 2.2).
195 About six years (March 2014 - 2020) of data from the 2A.GPM.DPR product (V06) was used.

196 **2.1.4 Reanalysis Data**

197 Tropopause temperature is needed for our IR algorithm. We used the tropopause
198 information output from the Modern-Era Retrospective Analysis for Research and Applications,
199 Version 2 (MERRA-2), instantaneous two-dimensional collections, hourly, single-level
200 diagnostics (MERRA2_400.inst1_2d_asm_Nx) product (Bosilovich et al., 2016). The MERRA-2
201 parameter ‘TROPT’ is a blended estimate of tropopause temperature (T_p) based on a
202 combination of the World Meteorological Organization (WMO) definition of the primary lapse-
203 rate tropopause (Grise et al., 2010) and equivalent potential vorticity. The tropopause data has a
204 spatial resolution of 0.625° x 0.5° longitude-latitude. The closest MERRA-2 grid in space and
205 time was assigned to each MODIS observation.

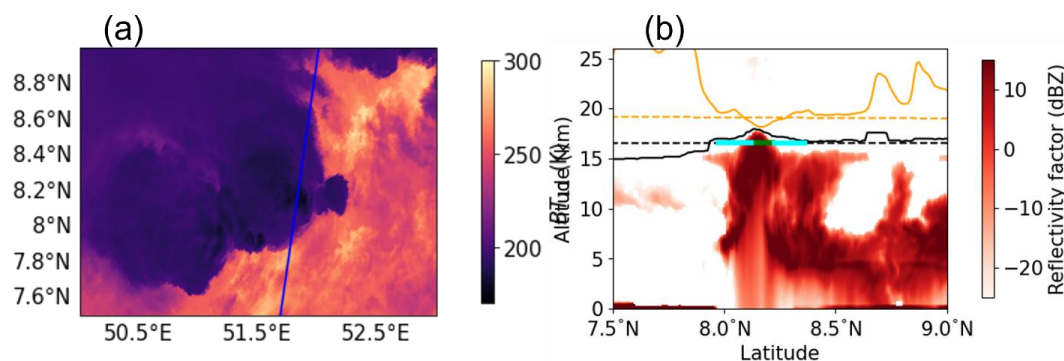
206 **2.2 OT Identification Algorithm**

207 **2.2.1 OT Selections from A-Train Observations**



208 The first step of the IR algorithm is to generate an OT training dataset. We manually
209 selected OT candidates around the world from 2007 and 2008 by visualizing the CPR reflectivity
210 factor from 2B-GEOPROF, topmost cloud top height from 2B-CLDCLASS-LIDAR, tropopause
211 information from MERRA-2 and the collocated T_{b11} from Aqua MODIS. For the CloudSat-
212 MODIS collocation, the nearest Aqua MODIS pixels were assigned to the CloudSat track. The
213 distance of the collocated CPR–MODIS pixels is usually less than 700 m, allowing these two
214 sensors to observe nearly the same cloud within one minute (Hong & Di Girolamo, 2020). OTs
215 were selected by visually inspecting the visualization rather than using a fix criterion. For
216 instance, Figure 1 shows an example of how we manually select OTs from this visualization.
217 Figure 1a displays that CloudSat overpassed a strong convective system with T_{b11} as low as 180
218 K. Figure 1b shows the curtain of the radar reflectivity factor from CloudSat for this convective
219 system, along with $T_{b11}/10$ (orange-solid line), cloud top height (black-solid line) and
220 tropopause information (orange-dash for tropopause temperature (T_p) divided by 10, and black-
221 dash for tropopause height) along the transect. As Figure 1b shows, in the convective core,
222 cloud top height is above the tropopause height, and the T_{b11} is colder than tropopause
223 temperature (T_p). This case is identified as an OT. In total, we have selected 209 OTs from A-
224 Train observations. Additionally, 78 non-OTs (NOTs) were also selected for model training. The
225 NOTs share very similar characteristics with OTs, i.e. T_{b11} is cold and has a local minimum, but
226 no overshoot top is observed from the visualization. Figure 2 shows very similar OT and NOT
227 T_{b11} distributions.

228



229

230 Figure 1. An OT case occurring at night over the Indian Ocean on June 1st, 2007: a) Brightness
231 temperature at 11 μm from Aqua MODIS, with blue line indicating the CloudSat track; b)
232 Vertical cross section of CloudSat radar reflectivity factor overlapped with MERRA-2
233 tropopause temperature divided by 10 (orange-dashed), tropopause height (black-dashed),
234 topmost cloud top height from 2B-CLDCLASS-LIDAR (black-solid), and $T_{b11}/10$ (orange-
235 solid). The green line in b indicates the OT region along CloudSat track determined by the
236 method from Marion et al. (2019), and the cyan line indicates the surrounding cirrus anvil.

237

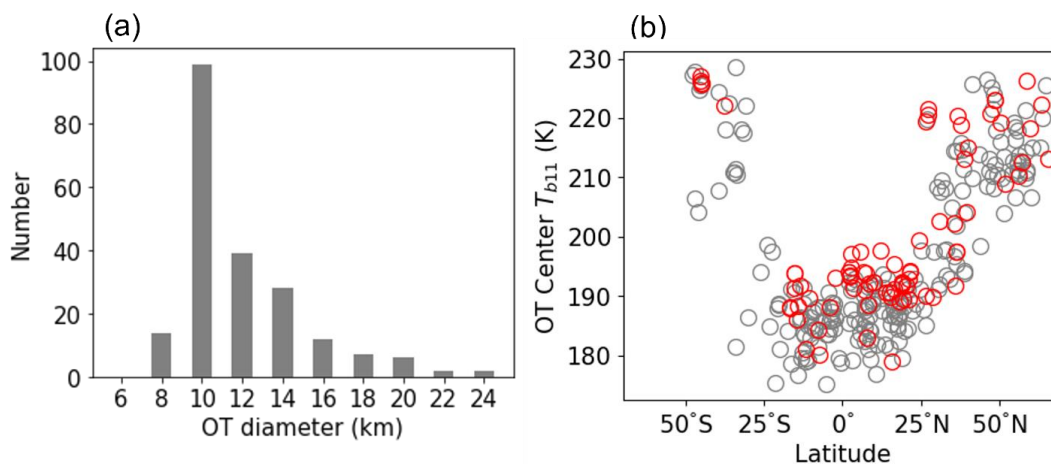
238 2.2.2 OT Edge and Cirrus Anvil



239 Once an OT was manually selected from the A-Train data, OT edges were determined
240 using the method described in Marion et al. (2019). Briefly, the local minimum T_{b11} along the
241 CloudSat track was set as the OT center. The 1-D second derivative along two radii along
242 CloudSat track ($\frac{d^2T_b}{dr^2}$) was computed using three-point Lagrange interpolation. The OT edges
243 along the two radii are defined as the first point where $\frac{d^2T_b}{dr^2} \leq 0$. With the OT edges determined,
244 the diameter of the OT candidate can be obtained. As an example, Figure 1b shows the OT
245 diameter in green, indicating that this method well catches the overshooting area.

246 The cirrus (Ci) anvil in this work was searched within 20 pixels around the OT center but
247 with the OT area excluded. Pixels starting from the OT edge and having $T_{b11} < 260$ K contribute
248 to the surrounding cirrus. A value of 260 K was used to screen cold clouds. This threshold has
249 been commonly adopted for screening high clouds associated with deep convection (Chung et
250 al., 2007; Tian et al., 2004). Figure 1b indicates the cirrus anvil in cyan. Once two edges of an
251 OT and its cirrus anvil were determined, the OT center T_{b11} , the mean brightness temperature for
252 the OT region ($\bar{T}_{b6.7}$ and \bar{T}_{b11}), the mean brightness temperature (\bar{T}_{b11}) for surrounding cirrus
253 averaged over two radii and the tropopause temperature (T_p) for the OT case were recorded to
254 construct the training dataset.

255 For the 209 OT candidates, all of them have their diameters less than 25 km, 180 OTs
256 (86%) have their diameters less than 15 km, and the peak in the OT diameter distribution is about
257 10 km (Fig. 2a), being agreeable with Bedka & Khlopenkov, (2016) which states that OTs are
258 typically less than 15 km in diameter. The T_{b11} of OT center along the CloudSat track is shown
259 in Fig. 2b which displays an asymmetric U-shape distribution along latitudes. Tropical OTs tend
260 to have their center T_{b11} less than 200 K, while mid-latitude OTs tend to have center T_{b11} colder
261 than 230 K. The NOT candidates share a very similar T_{b11} distribution with OTs. We rarely
262 found OTs outside the ± 60 -degree latitude range. In addition, for all OT candidates, WV-IRW
263 BTD ($T_{b6.7} - T_{b11}$) is found to be positive, and tropopause temperature is warmer than OT
264 center T_{b11} . For NOTs, they also have positive BTB, but 16% of them are warmer than
265 tropopause temperature. WV-IRW BTB and T_p are two important variables used for our IR
266 algorithm.



267
 268 Figure 2. (a) OT diameter distribution of the 209 OT candidates selected from 2007 and 2008 A-
 269 train data, and (b) brightness temperature at 11 μm of OT (grey) and NOT (red) center along
 270 CloudSat track.

271

272 2.2.3 Logistic Regression

273 Similar to Bedka & Khlopenkov (2016), a probability was generated for an OT
 274 candidate. The 209 OTs and 78 NOTs selected from A-Train observations served as inputs for
 275 the logistic model. The logistic regression is a statistical model that is used to model a certain
 276 event through assigning a probability between 0 and 1 such as classification of OT and NOT.
 277 The logistic model depends on several variables or predictors, shown as

$$278 \quad P = \frac{1}{1 + e^{-(b_0 + \sum_i^n b_i x_i)}} \quad , \quad (1)$$

279 where P is the probability of an OT candidate, b_0 is the constant, x_i is the variable and b_i
 280 represents the regressed coefficient.

281 Three MODIS-based variables were settled on after a series of tests to optimize the
 282 accuracy. They are x_1 - the difference between Ci anvil mean T_{b11} and OT center T_{b11} , x_2 - the
 283 difference of T_p and OT center T_{b11} , and x_3 - the difference of mean $T_{b6.7}$ ($\bar{T}_{b6.7}$) and mean T_{b11}
 284 (\bar{T}_{b11}) of OT. 156 OTs and 48 NOTs were used to train the model and the regressed results are
 285 summarized in Table 1. The total accuracy is about 84% when probability > 0.6 is predicted to
 286 be an OT. 53 OTs and 30 NOTs were used to validate the regressed model with a total accuracy
 287 about 82%.

288 Table 1. A summary of the regressed coefficients (significant at the 99% level) for the
 289 variables selected for OT detection used in Equation 1.

Variables	Coefficients for the variables
b_0	-3.2397



x_1 - difference between Ci mean T_{b11} and OT center T_{b11}	0.2075
x_2 - difference of tropopause T_p and OT center T_{b11}	0.3516
x_3 - difference of averaged OT $T_{b6.7}$ and averaged OT T_{b11}	0.4996

290

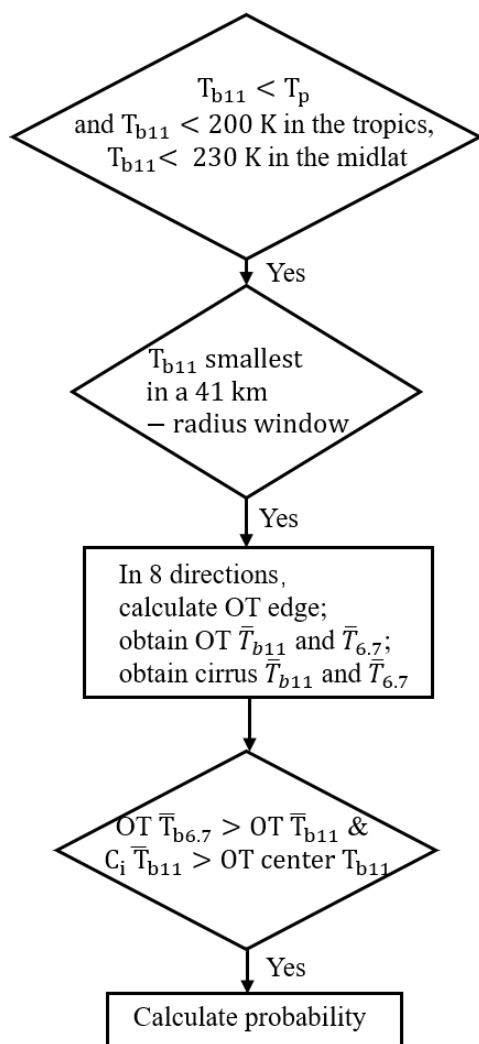
291 **2.2.4 Application of IR Algorithm to MODIS**

292

293 The logistic regression in Sect. 2.2.3 forms the basis of our IR algorithm, which aims to
294 automatically identify OTs from Terra and Aqua MODIS in the daytime and at nighttime. The
295 application of the IR algorithm starts from pixel search with T_{b11} colder than T_p , and T_{b11} less
296 than 200 K in the tropics (within 25° latitude) or less than 230 K in the midlatitudes (outside 25°
297 latitude). These T_{b11} thresholds selected to ensure that all OTs identified in Fig. 2b would pass
298 this first OT candidate selection criteria. If the pixel passed these thresholds and is a local
299 minimum in T_{b11} field in a 41 km x 41 km window, we continued to find the OT edges in eight
300 directions using the method by Marion et al. (2019), as mentioned in Sect. 2.2.2. OT \bar{T}_{b11} and
301 $\bar{T}_{b6.7}$ of the OT area are further computed over the pixels along eight radii once OT edges have
302 been determined. \bar{T}_{b11} of the surrounding cirrus is also computed in eight directions in the cirrus
303 area as defined in Sect. 2.2.2. When the surrounding cirrus \bar{T}_{b11} is warmer than OT center T_{b11}
304 and this OT case shows positive WV-IRW BTD (i.e. $\bar{T}_{b6.7} - \bar{T}_{b11} > 0$), OT probability is
305 calculated according to the logistic regression from Sect. 2.2.3. If one of the mentioned
306 conditions does not satisfy, the algorithm will search for next pixel. The flowchart of the IR
307 algorithm application is summarized in Fig. 3.

308 The window size of 41 km was adopted considering that 98% of the OTs (Fig. 2) have
309 their diameters less than 20 km according to A-Train observations (Sect. 2.2.2). This window
310 makes sure that two OT centers are at least 20 km apart and that enough pixels contribute to the
311 cirrus anvils. If multiple OTs occurred in the same window, the one with the coldest T_{b11} was
312 selected.

313



314

315

316 Figure 3. Flowchart for the application of IR algorithm to MODIS data. The \bar{T}_b represents the

317 mean of brightness temperature.

318

319 3. Validation of OT Detection Algorithm

320 3.1 Comparison with GPM

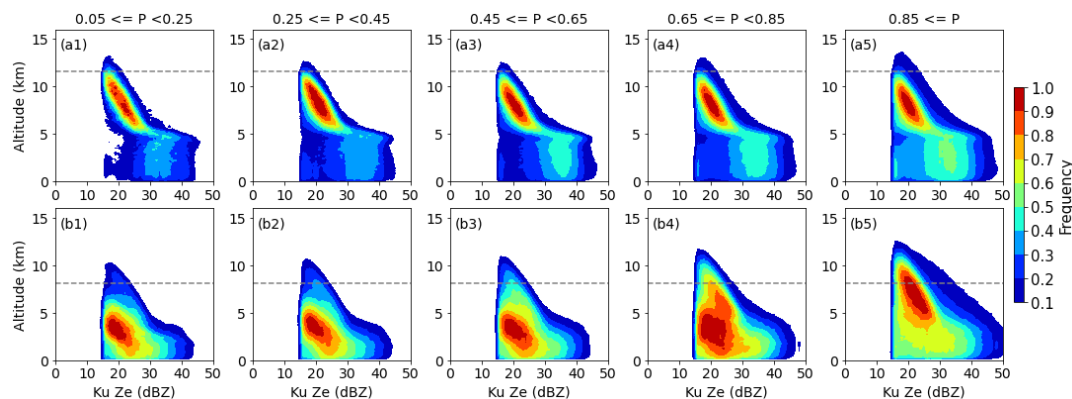
321 GPM has been demonstrated to be an effective tool in studying intense storms and
 322 overshooting top events (Hourngir et al., 2021; Liu et al., 2020; Liu & Liu, 2016). Here, we used
 323 the GPM observations for two purposes: To compare the performance of OT detection between
 324 GPM KuPR and Terra MODIS, and to investigate the cloud structure of detected OTs. The
 325 colocation between GPM KuPR and MODIS data was achieved when the time difference
 326 between them was within 5 minutes and the spatial difference between them was less than 10
 327 km. A 5-minute time window was used because the life cycle of OTs can be as small as several



328 minutes (Setvák et al., 2013). The collocating process was performed only when OT candidates
329 were identified from Terra MODIS. We obtained 6949 collocations for the period of March 2014
330 – December 2020.

331 Ku-band radar reflectivity factor (Z_e) in an area with a radius less than 40 km around the
332 colocated radar pixel were collected to construct the contour frequency by altitude diagram
333 (CFAD; Yuter & Houze, 1995). The parallax error between KuPR and MODIS could be more
334 than 20 km according to the method described in Wang et al. (2011). Also, OT diameter is likely
335 less than 20 km. An area with a 40 km radius for the colocated KuPR data is likely able to
336 encompass the OT event identified by MODIS. Figure 4 shows the CFADs contributed by all
337 (6949) colocated OT cases. The CFADs were segregated into 5 OT probability intervals for the
338 tropical and mid-latitude areas. As shown, the largest frequency occurs above 5 km in tropical
339 areas (Figs. 4a1-a5). As the OT probability increases, the frequency increases for large Z_e (> 30
340 dBZ) below 5 km. In the midlatitudes (Figs. 4b1-b5), higher frequency of the Z_e occurs below 5
341 km when OT probability is less than 0.85. For those OT cases with $P > 0.85$, large frequency is
342 mostly above 5 km, and large Z_e (> 30 dBZ) occurs more frequently below 5 km. With an
343 analysis of DPR rain type product, we noticed that the large Z_e (e.g. > 30 dBZ) below 5 km tend
344 to associate with convective rain in both the tropics and midlatitudes. An increase of convective
345 rain in the CFADs with larger OT probability indicates more likely OT occurrence. These
346 CFADs demonstrate that the probability generated from our IR algorithm indicates storm
347 intensity and a confidence level of OT detection.

348



349

350 Figure 4. Contoured frequency by altitude diagram, showing the frequency normalized by the
351 maximum bin of radar reflectivity. Data were binned at 1dBZ intervals at each level. The upper
352 upper panels are for the tropics (within 25° latitude), and the lower panels are for the midlatitudes
353 (between 25° and 60° latitude). The dashed lines in upper and lower panels represent the mean
354 tropopause height in the tropics and in the midlatitudes, respectively, derived from MERRA-2.
355

356 To compare the performance of OT detection between GPM and MODIS, we need to
357 determine when GPM detects an OT. If the maximum altitude of 15 dBZ in the 40-km radius
358 area was higher than 2 km below the MERRA-2 tropopause, an OT flag was assigned to the
359 colocated GPM pixel. Previous studies also adopted a level below the tropopause as the OT

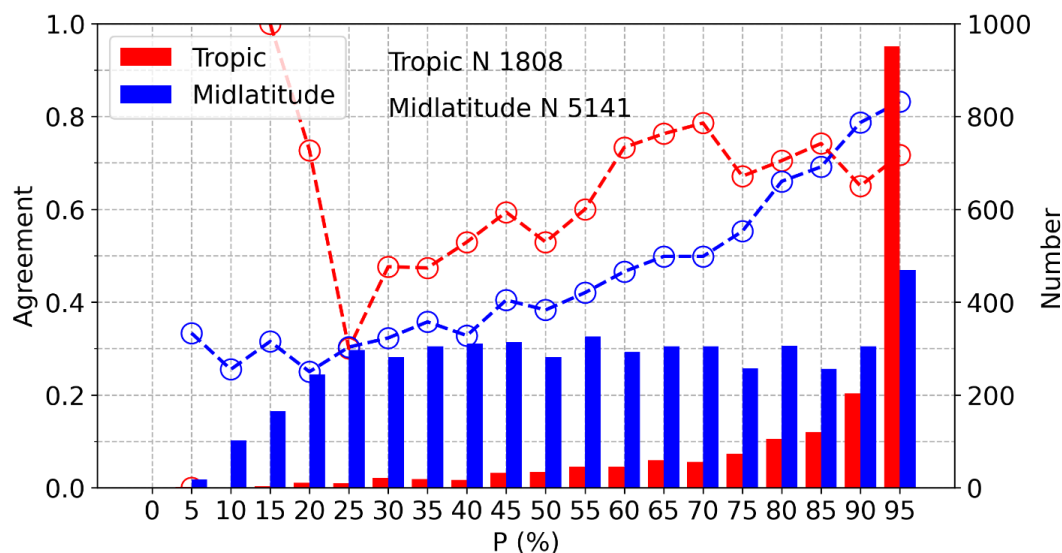


360 reference considering the tropopause height variability (Sun et al., 2019; Zhuge et al., 2015).
 361 Here, 2 km was selected due to an agreement of 67% between MERRA-2 and ERA-5 tropopause
 362 height (from ECMWF-AUX (Partain, 2007)) for the 287 OTs and NOTs cases used in Sect. 2.
 363 Once OT flags were assigned to the collocated GPM cases, agreement of OT detection between
 364 MODIS and GPM was calculated for a wide range of OT probability generated by the IR
 365 algorithm. The agreement is expressed as

$$366 \quad \textit{Agreement} = \frac{N(H > H_p - 2 \cap P_1 < P < P_2)}{N(P_1 < P < P_2)} \quad (2)$$

367 where H is the maximum altitude (in km) of 15 dBZ in the 40-km radius area, H_p is tropopause
 368 height from MERRA-2, and N is the OT numbers with OT probability between P_1 and P_2 .

369 Figure 5 shows the agreement in OT detection between MODIS and GPM which
 370 increases with OT probability. In the tropics, the agreement is about 70% when $P > 90\%$ with
 371 enough samples, while in the midlatitudes, the agreement is larger than 80% when $P > 0.90$.
 372
 373



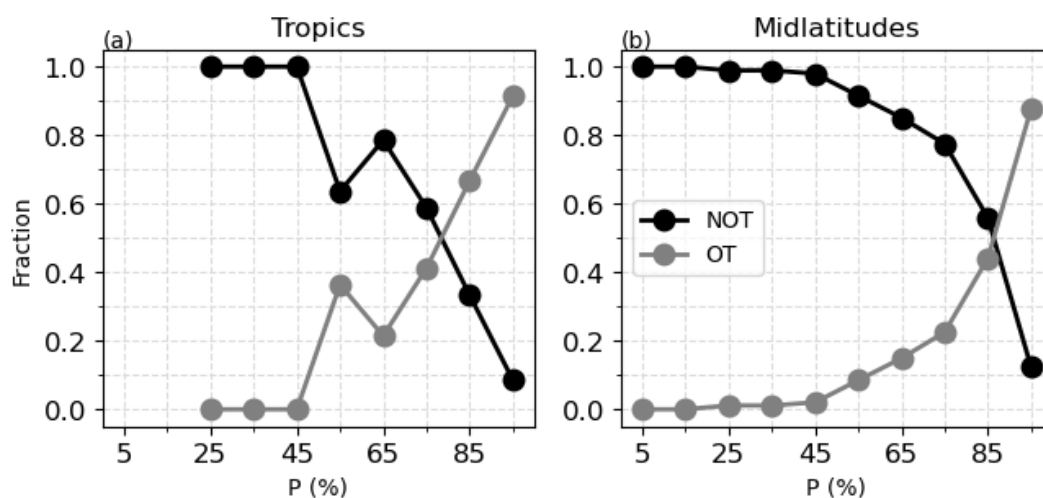
374
 375 Figure 5. Comparison of OT detection between GPM and Terra MODIS. Curves represent
 376 agreement of OT detection between MODIS and GPM in various probability intervals, red for
 377 the tropics and blue for the midlatitudes; the numbers of potential OT candidates are shown in
 378 bars. N stands for sample number.

379
 380 **3.2 Manual Check**

381 As a complement to GPM-MODIS comparison for assessing IR algorithm accuracy, we
 382 manually checked 1158 daytime OT candidates (selected randomly across the year) from Terra
 383 MODIS from 2018-2020. These OT candidates are with a wide range of probability. OT and
 384 NOT flags were assigned to the candidates by visually inspecting the IR and visible images from
 385 the NASA Worldview website (<https://worldview.earthdata.nasa.gov>). The fraction of OT and



386 NOT segregated at a 0.1 probability (generated from the IR algorithm) interval was calculated
387 (Fig. 6). As displayed, the fraction of OT substantially increases when the probability is greater
388 than 0.8 in both the tropics and midlatitudes. In the tropics, the fraction of NOT is about 30%
389 when P is between 0.8 and 0.9, and it decreases to about 10% when $P \geq 0.9$. In the midlatitudes,
390 when the P is small (e.g. < 0.8), NOT fraction is higher than OT fraction. Only when $P \geq 0.9$,
391 NOT fraction drops to about 10%. With a manual check of about 900 OT candidates selected
392 from July, 2018 Aqua MODIS, similar accuracy was obtained ($\sim 90\%$ when $P \geq 0.9$). This
393 manual check is consistent with the OT comparison with GPM as discussed in Sect. 3.1, i.e.,
394 higher OT probability gives higher confidence in our IR algorithm for OT detection.
395



396
397 Figure 6. Fraction of OT candidates with a wide range of probability in the Tropics (a), and
398 midlatitudes (b). X-axis shows in a probability interval of 0.1.
399

400 Overall, we choose a P threshold of 0.9 in both the tropical and mid-latitude regions,
401 which assures a total detection accuracy of ~ 0.9 (better than 0.9 in the tropics and slightly lower
402 than 0.9 in the midlatitudes) as demonstrated in Sect. 3.2. For the Terra MODIS data from
403 February 2000 to December 2021 and Aqua MODIS data from July 2002 to December 2021, OT
404 candidates that pass the probability threshold of 0.9 account for about 30% and 35%,
405 respectively, of all candidates over regions within $60^{\circ}\text{S} - 60^{\circ}\text{N}$. In the tropics, 58% (62%) of the
406 candidates from Terra (Aqua) MODIS have $P > 0.9$, while in the midlatitudes, only 13% (16%)
407 of the candidates were retained. Note that we do not consider polar regions as our manual
408 selected OTs in Sect. 2.2 rarely occur outside 60° latitudes.

409 4. Results and Discussions

410 In this section, we show an OT climatology of those OT candidates with $P \geq 0.9$.
411 Candidates with $P < 0.9$ were excluded due to a high fraction of NOTs as discussed in Sect. 3.

412 4.1 Case Analysis



413 Before showing the climatology, we first show four cases including all OT candidates
414 with a variety of probabilities for a detailed view of the performance of our IR algorithm in
415 different storm environments.

416 Figure 7 shows visible reflectance overlapped with OT centers, which are colored by OT
417 probability. T_{b11} for each case is also shown overlapped with the pixels colder than tropopause
418 and having positive WV-IRW BTD (marked in white). The rain type and precipitation rate
419 averaged between 2-4 km from GPM are shown in the third and fourth columns.

420 Overshooting tops in tropical cyclones (TC) are common. They are found closely linked
421 to intense convection and rapid intensification in TCs (Griffin, 2017; Monette et al., 2012; Tao
422 and Jiang, 2013). Figures 7a1-7a4 displays a tropical cyclone over the north Indian Ocean on
423 Nov. 08th, 2019. OTs are detected in the area with very cold T_{b11} associated with strong
424 convection and precipitation as GPM identifies convective rain type near OT areas. Our
425 algorithm usually generated high probability for OT candidates detected in TCs.

426 In the mesoscale convective system case (Figs. 7b1-b4), OTs are detected in the clusters
427 that associate with cold T_{b11} and positive WV-IRW BTD. Strong precipitation is indicated by
428 GPM. Our algorithm also usually produces high probability for OTs detected in mesoscale
429 convective systems.

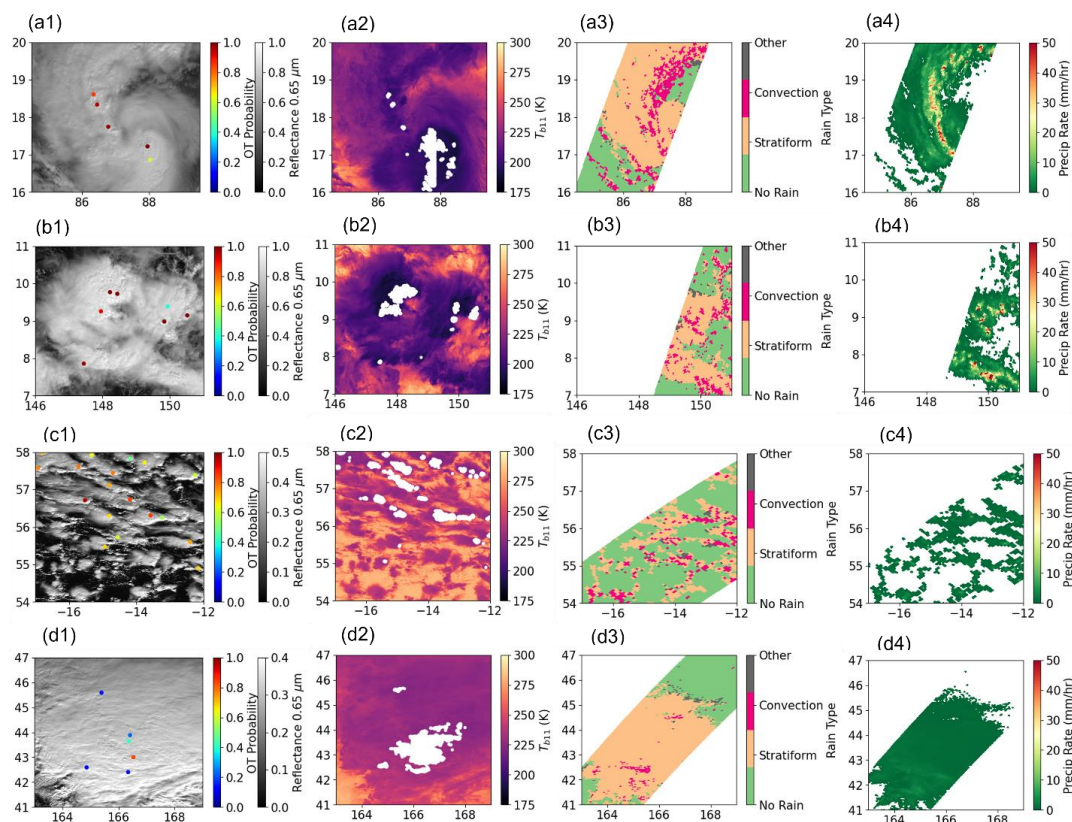
430 Cold air outbreaks can produce shallow convection when cold air blows from frozen
431 surfaces to warmer ocean. The Cold-Air Outbreaks in the Marine Boundary Layer Experiment
432 (COMBLE) found that these convective clouds are commonly lower than 5 km associated with
433 updrafts of 4-5 m s^{-1} (Geerts et al., 2022). In the cold air outbreaks, the tropopause is low, which
434 is often at a level below 500 hPa (Papritz et al., 2019; Terpstra et al., 2021), compared to the
435 mid-latitude tropopause climatology of 200-300 hPa (Wilcox et al., 2012). Thus, updrafts in
436 these shallow convective clouds are able to penetrate the tropopause and produce overshooting
437 cloud tops. In the third case (Figs. 7c1-c4), overshooting tops from convective turrets over the
438 north Atlantic within a cold air outbreak occur with high OT probability. GPM identifies
439 convective precipitation surrounding by stratiform precipitation in these shallow convective
440 clouds. Our method allows for the detection of these OTs that can occur in unstable conditions
441 with shallow tropopauses.

442 Mid-latitude winter cyclones are associated with mostly stratiform cloud systems
443 (Stewart et al., 1998), as also demonstrated by the GPM rain type that shows mostly stratiform
444 precipitation (Figs. 7d1-d4). The tops of stratiform clouds associated with the fronts usually
445 reach to tropopause without no strong convective cores. However, they can occur associated with
446 lightning and heavy precipitation when fueled by potential instability, with updrafts of 6-8 m s^{-1}
447 (Murphy et al., 2017; Rauber et al., 2014, 2015). Our algorithm detects OT candidates in this
448 cloud system usually with low probability which will be excluded in our OT climatology
449 analysis except for some rare situations with high OT probability.

450

451

452



453

454 Figure 7. Four selected cloud systems with OTs detected by our IR algorithm. First column
 455 shows the reflectance at $0.65 \mu\text{m}$ (dots indicate OT probability), the second column shows the
 456 brightness temperature at $11 \mu\text{m}$ (white dots indicate pixels colder than tropopause temperature
 457 and having positive WV-IRW BTD). Columns 3 and 4 represent rain type and precipitation rate
 458 from GPM, respectively. Case 1 (a1-a4) for the tropical cyclone over Bay of Bengal on Dec. 8th,
 459 2019, case 2 (b1-b4) for a mesoscale convective system over East of Philippines on Dec. 03rd,
 460 2019, case 3 (c1-c4) (Mar. 10th, 2019 over the north Atlantic Ocean) for shallow post-frontal
 461 convection, and case 4 (d1-d4) (Dec. 15th, 2018 over the north Pacific Ocean) for the cloud
 462 system in the midlatitude cyclone.

463

464 4.2 Near Global OT Distributions

465 Figure 8 shows the seasonal distributions of OT occurrences contributed by those OT
 466 candidates with $P \geq 0.9$, derived from Terra (February 2000 - 2021) and Aqua (July 2002 -2021)
 467 MODIS. As displayed, OT distributions and their seasonal variations follow the expected pattern
 468 based on the known climatology of convection (Alcala and Dessler, 2002; Funk et al., 2015). In
 469 JJA (Fig. 8b), as revealed by both Aqua and Terra MODIS, OTs primarily distribute over north
 470 of the equator in the intertropical convergence zone (ITCZ). A large population of OTs over
 471 India, Bay of Bengal, and southeast Asia are associated with the summer South Asian monsoonal



472 system. Our algorithm also detects considerable OTs in Asia between 45°-60° latitudes and in
473 Europe, where severe storms occur in local summer (Groenemeijer et al., 2017; Shikhov et al.,
474 2021). These profound OTs agree with what GPM has found in the northern mid and high
475 latitudes (Liu et al., 2020). However, a T_{b11} threshold of 215 K usually filter out these OTs (e.g.
476 Li et al., 2022). Another hot spot of OTs occurs in central North America. In addition, we
477 observe a narrow belt of large OT occurrences over the west Atlantic Ocean, which are
478 associated with the location of tropical cyclones.

479 Aqua MODIS also shows frequent OT occurrences over the southeastern United States
480 associated with the afternoon convection. In regions over the U.S. southwest and northwestern
481 Mexico, OTs are detected associated with the summer North America Monsoon (Adams and
482 Comrie, 1997).

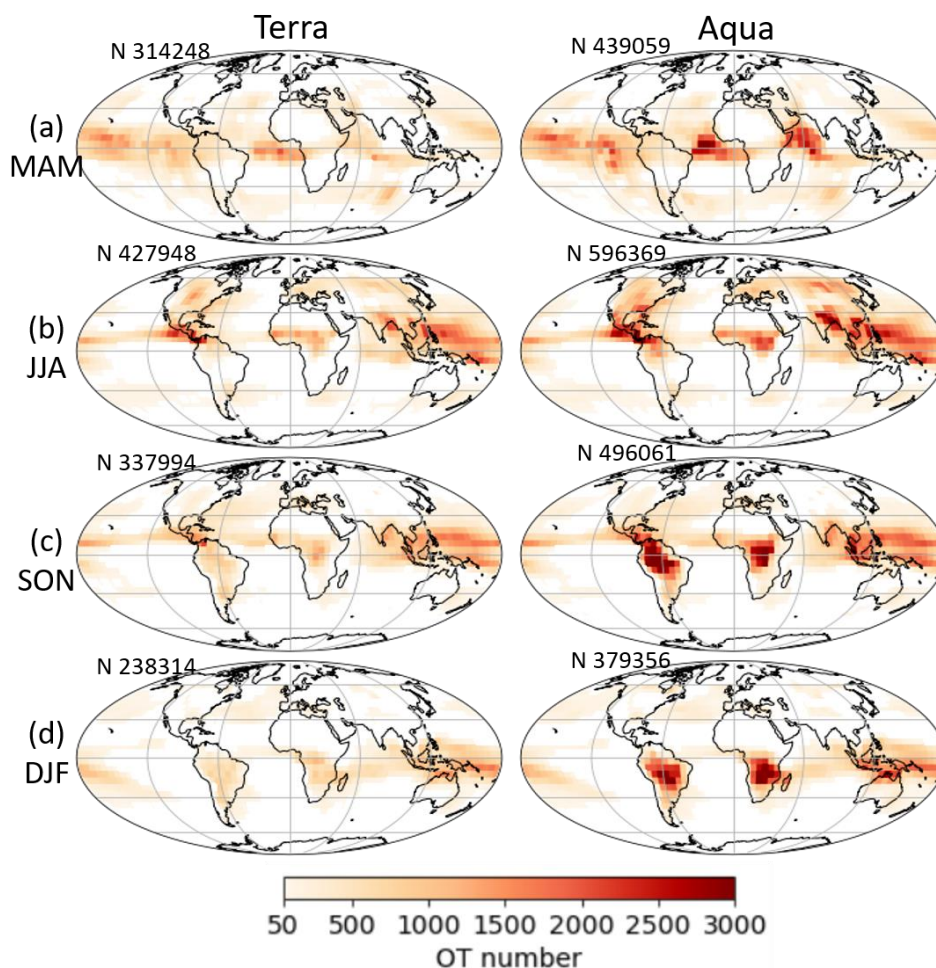
483 During DJF (Fig. 8d), OT occurrences are about 44% at 10:30 LT (Terra equator crossing
484 time) and 36% at 1:30 LT (Aqua equator crossing time) $((N_{\text{summer}}-N_{\text{winter}})/N_{\text{summer}})$ less
485 than that in JJA. OTs are primarily located over the Southern Hemisphere as the ITCZ moves to
486 the south of the equator. A large number of OTs are detected by Aqua MODIS over tropical and
487 subtropical South America and Africa. In the Northern Hemisphere, OTs become infrequent
488 over land. Note that ice clouds have an occurrence frequency about 70% over mid- and high-
489 latitude Asia during winter (e.g. Hong and Liu 2015), which often pose challenges for OT
490 identification. These cold ice clouds are rarely classified as OTs in our analysis, demonstrating
491 the ability of our IR method to avoid the misclassification of cold ice clouds to OTs. In contrast,
492 over the mid-latitude ocean in winter, we see some OT occurrences. These OTs are associated
493 with isolated convective clouds occurring in the cold air outbreaks as discussed in Sect. 4.1.
494 These OTs are also observed over Southern Ocean during JJA (Austral winter). We also notice a
495 small number of OTs extending from northwest to southeast North America in DJF. These OTs
496 are associated with the convection in winter mid-latitude cyclones as discussed in Sect. 4.1.

497 Convective activity over land is weak at Terra overpass time in the morning (~ 10:30 am)
498 and it becomes more frequent and intense in the afternoon when Aqua satellite overpasses. This
499 is revealed by the differences of OT occurrences between Terra and Aqua, indicating the
500 variability of OT diurnal cycles.

501

502

503



504

505 Figure 8. The global distributions of OT occurrences derived from Terra and Aqua MODIS in
506 four seasons: (a) March-April-May (MAM), (b) June-July-August (JJA), (c) September-October-
507 November (SON) and (d) December-January-February (DJF). Grid resolution is 5° longitude by
508 5° latitude. Samples in grids less than 50 are shown in white. N over the upper right corner in
509 each panel stands for sample number,

510 4.3 OT Diurnal Cycle

511 This section discusses OT diurnal cycles based on the four observation times by Aqua
512 and Terra MODIS. The OT occurrences in the daytime (~10:30 am and ~1:30 pm) and at night
513 (~10:30 pm and ~1:30 am) are displayed in Fig. 9. According to previous studies on the diurnal
514 cycle of convection (Alcala and Dessler, 2002; Nesbitt and Zipser, 2003), convective activity
515 over land is generally more frequent and intense in the afternoon and evening compared with
516 early morning. Over oceans near the coastlines, morning convection is more intense (Johnson,
517 2011). In agreement with previous studies, we observe the most OT occurrences at about 1:30

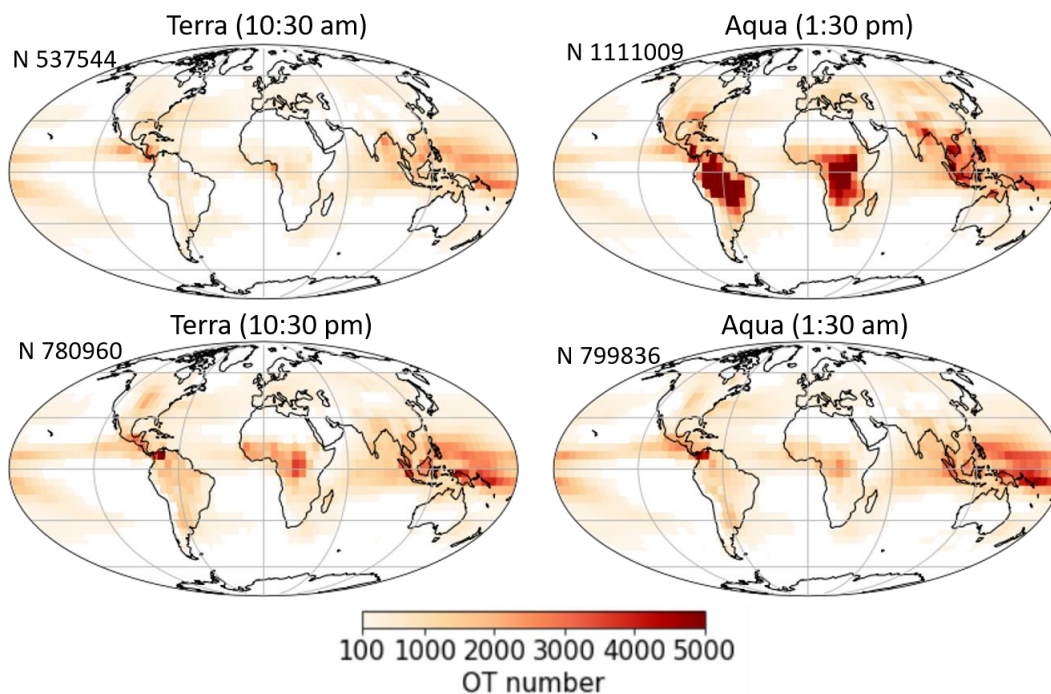


518 pm from Aqua MODIS, primarily contributed by land areas including tropical South America,
519 tropical Africa, the Maritime continent and the southern foothills of Himalayas. Over Bay of
520 Bengal, South China Sea, Gulf of Guinea, Gulf of Mexico, Panama and its surrounding regions,
521 OTs away from coastlines have been observed, commencing in the morning (~ 10:30 am) and
522 continuing into afternoon (~ 1:30 pm). Over the west Pacific Ocean, OTs occur the most around
523 midnight at ~ 1:30 am.

524 To better view the OT diurnal cycles, Figure 10 shows when maximum and minimum OT
525 occurrences occur in the four-observation time. Diurnal cycle intensity defined by the difference
526 of maximum and minimum OT numbers normalized by the mean is shown in Figs.10 e and f. As
527 expected (Figs. 10a and 10b), the largest OT occurrences over land occur at about ~ 1:30 pm
528 except for central North America and west Africa where have a midnight maximum in
529 convection during JJA (Janiga and Thorncroft, 2014; Nesbitt and Zipser, 2003; Tian et al., 2005).
530 Ocean areas consistently have maximum OT occurrence at ~ 1:30 am (Figs.10a and 10b). The
531 minimum OT occurrence over land usually occurs at ~ 10:30 am except for some regions over
532 North America and Asia where the minimum OT occurrence is at ~1:30 am during JJA (Fig.
533 10c). The time for minimum OT occurrence over ocean has a large variability.

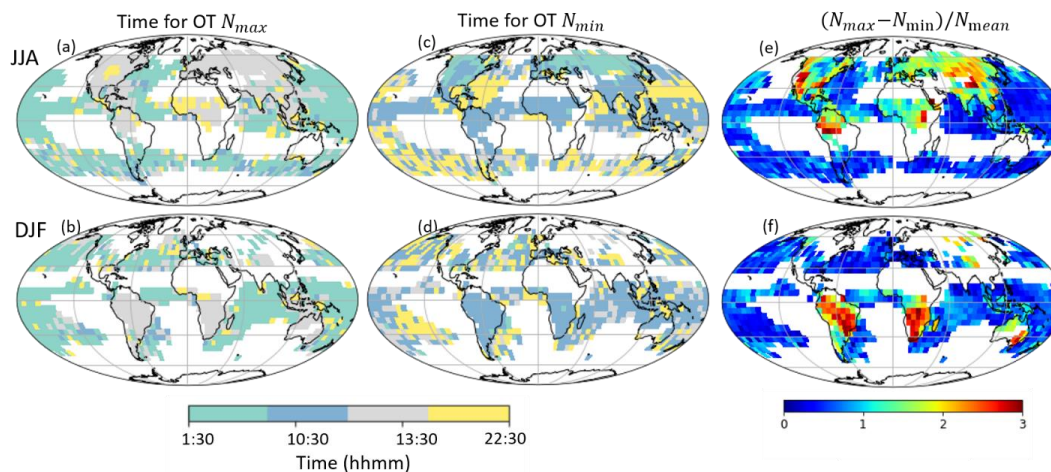
534 The diurnal cycles of OT occurrences over ocean are generally weak (Figs. 10e and 10f),
535 being consistent with previous convection diurnal cycle analysis (Alcala & Dessler, 2002; Liu &
536 Zipser, 2005; Nesbitt & Zipser, 2003). In contrast, the OT diurnal cycles over land are much
537 stronger than over ocean. Strong regional variations are also discovered over land areas.
538 Relatively strong OT diurnal cycles are found during JJA over southwest North America,
539 southeast United States, Tibetan High, tropical South America, and during DJF over southeast
540 Australia, tropical and subtropical South America and subtropical Africa. Relatively weak
541 diurnal cycles over land are observed in central North America and west Africa in JJA. Strong
542 regional variations in OT diurnal cycle over land are consistent with previous studies based on
543 convection and precipitation that demonstrate the diurnal cycles are complicatedly modulated by
544 land-sea contrast, topography, coastline curvature and response to solar heating to surface
545 (Janiga and Thorncroft, 2014; Tian et al., 2005).

546



547

548 Figure 9. The global distributions of OTs at four observation times. Grids with OT number < 100
 549 are shown in white. N stands for sample number,



550

551 Figure 10. Panels a-d are for the time when maximum and minimum OT occurrence occurs
 552 across the four-observation time. Panels e-f are for diurnal intensity of OT occurrences, defined
 553 as the difference of maximum and minimum OT occurrences, normalized by the mean. Only
 554 when the minimum OT occurrences > 10 in each 5°x5° grid, data is shown.



555 4.4 Land-Sea Contrast

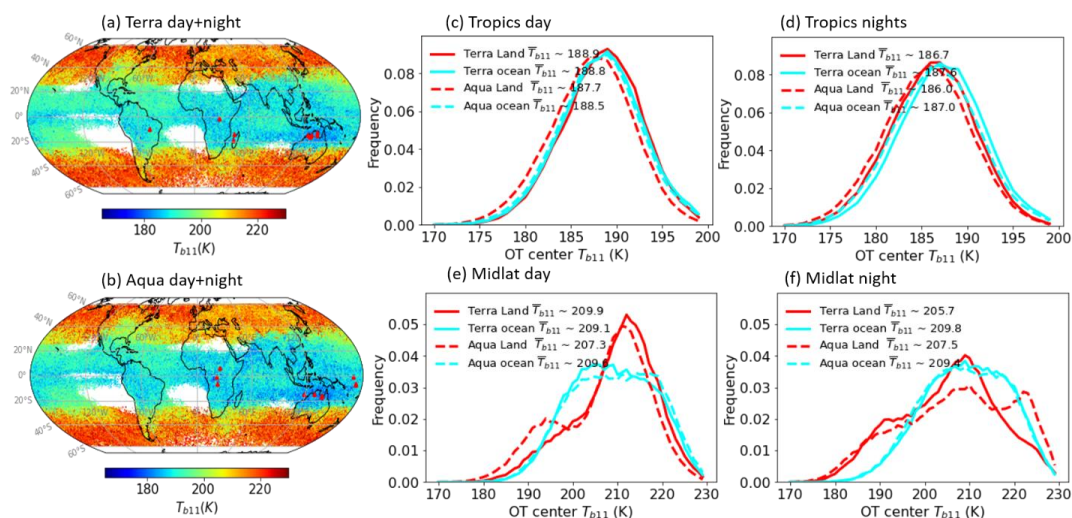
556 From the diurnal cycle analysis in Sect. 4.3, we have noticed some land-sea contrast in
557 OT characteristics. For instance, OTs occur more frequently in the afternoon over land, whereas
558 they are more frequent at midnight over ocean, and OT occurrence diurnal cycle is stronger over
559 land than over ocean. In this section, attention is placed on OT center T_{b11} , which indicates
560 storm intensity. By checking the geospatial distributions of OT center T_{b11} , we observe
561 extremely cold OT center T_{b11} (e.g. < 180 K) appearing over the tropical regions, including
562 regions near northern Australia, east of Papua New Guinea, India and nearby Arabian sea,
563 tropical and subtropical Africa, and tropical and subtropical South America, derived from both
564 Aqua and Terra MODIS (Figs. 11a and 11b). The locations of cold OTs are also aligned with the
565 places where occur intense convection based on TRMM (Zipser et al., 2006).

566 Particularly, the first 10 coldest OTs (marked in red triangles and summarized in Table 2)
567 from Aqua and Terra MODIS nearly occur in Southern Hemisphere with more cases over land
568 than over ocean. The top 10 OTs from Aqua are colder than 167 K with the coldest OT of 165.6
569 K over east of Papua New Guinea, whereas Terra shows the coldest OT of 167.2 K occurring in
570 northern Australia. This finding agrees with the cold OT distributions discussed in Proud &
571 Bachmeier, 2021, which states that an extremely cold tropopause coupled to an energetic
572 overshooting top produced such a cloud top temperature.

573 Additionally, Figs. 11a and 11b reveal colder OTs over land than over ocean at the same
574 latitudes. By checking the probability density distributions (PDFs) of OT center T_{b11} , we find
575 that land-sea contrast in OT T_{b11} also relies on diurnal cycle. In the daytime morning ($\sim 10:30$
576 am) when convection over land is weak, T_{b11} over land is slightly warmer than over ocean in
577 both the tropics and midlatitudes (Figs. 11c and 11e). Land-sea contrast in T_{b11} is small at this
578 time. At $\sim 1:30$ pm as convection becomes stronger over land, T_{b11} over land is on average 0.8 K
579 and 2.3 K colder than over ocean in the tropics and midlatitudes, respectively (Figs. 11c and
580 11e). At nighttime (Figs. 11d and 11f), land-sea contrast in T_{b11} becomes stronger than in the
581 daytime. In the tropics, T_{b11} over land is about 1 K on average colder than that over ocean,
582 whereas in the midlatitudes, it is about 2 K colder over land than over ocean.

583 Our findings indicate that OTs over land are more intense than over ocean except for the
584 early morning ($\sim 10:30$ am) when convection over land is weak. These findings agree with
585 previous studies that have shown more intense convection over land area, associated with
586 stronger updrafts than the oceanic counterpart (Jeyaratnam et al., 2021; Liu & Zipser, 2005).

587



588

589 Figure 11. a and b are for spatial distributions of OT center T_{b11} . Panels c-f are for OT center
 590 T_{b11} PDFs in the tropics and midlatitudes, segregated in day and nighttime.

591 Table 2. Summary of the top 10 coldest OTs from Terra and Aqua, respectively.

	Terra				Aqua			
	$T_{b11}(K)$	Location(lon,l at)	Time ¹	D/N ²	$T_{b11}(K)$	Location(lon,l at)	Time	D/ N
1	167.2	129.75,-14.54	2016365.13 50	N	165.6	172.65,-6.66	2018365.14 15	N
2	167.6	128.62,-15.76	2006023.14 10	N	166.4	169.81,-0.99	2018365.14 10	N
3	167.6	125.47,-14.62	2014004.02 05	D	166.5	21.34,-0.74	2015082.00 30	N
4	167.8	27.28,-1.46	2013023.20 20	N	166.6	22.29,-6.15	2020053.23 55	N
5	167.8	-48.54,-9.98	2013029.01 30	N	166.7	172.54,-7.35	2018365.14 15	N
6	167.8	136.12,-14.72	2019003.13 20	N	166.7	138.75,-17.12	2018332.04 20	D
7	167.8	44.58,-19.05	2006074.19 35	N	166.8	138.71,-15.78	2012080.16 25	N
8	168.1	44.63,-13.74	2004023.19 25	N	166.8	129.75,-14.64	2003020.05 00	D
9	168.3	135.39,12.79	2008006.14 05	N	166.9	118.45,-14.93	2016359.06 00	D
10	168.3	128.49,-16.31	2018001.14 05	N	166.9	24.93,5.63	2008123.11 40	D

592 1. Time in the format of year.day.hhmm



593 2.D for day and N for night

594

595 5. Conclusions

596 To utilize about two-decade MODIS records in study of convective overshooting tops,
597 we developed an IR algorithm to detect OTs from MODIS. The resultant OT climatology was
598 used to understand OT regional and seasonal distributions, OT diurnal cycles and OT land-sea
599 contrast.

600 The approach to detect OTs uses IR radiances from MODIS water vapor ($6.7 \mu\text{m}$) and
601 window ($11 \mu\text{m}$) channels. This approach was built upon the logistic regression which was
602 trained and validated with ~ 287 OT candidates identified from the combined CloudSat-
603 CALIPSO-MODIS (CCM) data. As demonstrated by six-year collocated GPM observations, the
604 OT probability generated by the IR algorithm indicates storm intensity and represents a
605 confidence level of OT detection. When OT probability is higher than 0.9, the accuracy for OT
606 detection is better than about 0.9 as validated by manual check.

607 The global and seasonal distributions of OT occurrences follow the expected pattern
608 based on the known climatology of deep convection and precipitation, shifting with the ITCZ
609 and monsoonal systems. Frequent OTs are also observed over central North American, Europe,
610 northern Asia and the northwest Atlantic Ocean in summer. Our OT climatology also includes
611 those OTs observed in the shallow convection over the mid-latitude ocean during winter cold air
612 outbreaks.

613 MODIS observations at four different time were used to derive part of the OT diurnal
614 cycle. The diurnal cycle follows the known diurnal cycle of convection: The most OT
615 occurrences are observed at about 1:30 pm (ECT) over most land area, including tropical and
616 subtropical South America, tropical and subtropical Africa, southeast North America, foot of
617 Himalayas and Maritime continent, etc. Over ocean, maximum OT occurrences are usually at
618 around midnight ($\sim 1:30$ am) except for offshore ocean. OT occurrences in the morning ($\sim 10:30$
619 am) over coastal ocean are apparent which continue to the afternoon at $\sim 1:30$ pm. Minimum OT
620 occurrences are usually at $\sim 10:30$ am over land. Over ocean, however, minimum occurrences
621 can be at any time except 1:30 am. Also, the OT diurnal cycle is stronger and more varied over
622 land than over ocean.

623 Jeyaratnam et al., (2021) indicated that tropical convection is deeper than mid-latitude
624 convection. This is also revealed by the midlatitude-tropics contrast in OT center T_{b11} shown in
625 this study, i.e. tropical OTs are colder than mid-latitude OTs. In the tropics, the the OT center
626 T_{b11} tends to be colder over land than over ocean accept at $\sim 10:30$ am when convection over
627 land is weak. Also, the top 10 coldest OTs from either Terra or Aqua mostly occur over land
628 These results agree with previous studies that have confirmed that tropical land areas exhibit
629 more intense overshooting convection than the tropical oceans (Alcala & Dessler, 2002; Liu &
630 Zipser, 2005). Mid-latitude OTs have stronger land-sea contrast in T_{b11} than in the tropics with
631 OTs over land being 2.3, 4.1 and 1.9 K colder than over ocean at about 1:30 pm, 10:30 pm and
632 1:30 am, respectively.

633 This study has displayed a comprehensive analysis of OT occurrences for the first time
634 using MODIS data that has a better spatial resolution (1 km) and covers the longest time period



635 than previous OT climatologies that were derived from either GPM, GOES or AMSU-B. Our
636 ongoing work seeks to use this OT climatology to quantify OT aera, which will lead to valuable
637 insights into intense updraft size distributions in deep convection over the globe.

638 **Data availability**

639 CloudSat data including 2B-GEOPROF, 2B-CLDLASS-LIDAR and ECMWF-AUX, were
640 downloaded from <https://www.cloudsat.cira.colostate.edu/>.

641 GPM radar data is available at https://disc.gsfc.nasa.gov/datasets/GPM_2ADPR_07/summary.

642 MODIS data is available at <https://ladsweb.modaps.eosdis.nasa.gov/>.

643 MERRA-2 data can be downloaded at

644 <https://goldsmr4.gesdisc.eosdis.nasa.gov/data/MERRA2/M2I1NXASM.5.12.4/>.

645 **Author contribution**

646 YH, JT, SN and LDL conceived this study. YH performed the analysis, collected data, and wrote
647 the manuscript. SN collected data, helped with data analysis and edited the manuscript. JT
648 helped with interpretation of results and edited the manuscript. LD joined result discussions and
649 edited the manuscript.

650 **Competing interests**

651 The authors declare that they have no conflict of interest.

652 **Acknowledgements**

653 This work was mainly supported by the NASA award 80NSSC20K0902. The authors would like
654 to acknowledge Dr. Guangyu Zhao for his help in downloading the Terra MODIS data. We
655 thank the CloudSat Data Processing Center for providing CloudSat products, including 2B-
656 GEOPROF, 2B-CLDCLASS-LIDAR and ECMWF-AUX. We thank the Level-1 and
657 Atmosphere Archive & Distribution System (LAADS) Distributed Active Archive Center
658 (DAAC) for offering MODIS data (LAADS DAAC, 2022). We also acknowledge the NASA's
659 Goddard Earth Sciences Data and Information Services Center (GES DISC) for archiving
660 MERRA-2 data and GPM data (Iguchi and Meneghini 2021).

661

662 **References**

663 Ackerman, S. A.: Global satellite observations of negative brightness temperature differences
664 between 11 and 6.7 μm , *J. Atmos. Sci.*, 53(19), 2803–2812, doi:10.1175/1520-
665 0469(1996)053<2803:GSOONB>2.0.CO;2, 1996.

666 Adams, D. K. and Comrie, A. C.: The North American Monsoon, *Bull. Am. Meteorol. Soc.*,
667 78(10), 2197–2213, doi:10.1175/1520-0477(1997)078<2197:TNAM>2.0.CO;2, 1997.

668 Alcala, C. M. and Dessler, A. E.: Observations of deep convection in the tropics using the
669 Tropical Rainfall Measuring Mission (TRMM) precipitation radar, *J. Geophys. Res. Atmos.*,
670 107(24), doi:10.1029/2002JD002457, 2002.

671 Astin, I., Di Girolamo, L. and Van De Poll, H. M.: Bayesian confidence intervals for true



- 672 fractional coverage from finite transect measurements: Implications for cloud studies from space,
673 *J. Geophys. Res. Atmos.*, 106(D15), 17303–17310, doi:10.1029/2001JD900168, 2001.
- 674 Barnes, W. L., Pagano, T. S. and Salomonson, V. V.: Prelaunch characteristics of the moderate
675 resolution, *IEEE Trans. Geosci. Remote Sens.*, 36, 1088–1100, 1998.
- 676 Bedka, K., Brunner, J., Dworak, R., Feltz, W., Otkin, J. and Greenwald, T.: Objective satellite-
677 based detection of overshooting tops using infrared window channel brightness temperature
678 gradients, *J. Appl. Meteorol. Climatol.*, 49(2), 181–202, doi:10.1175/2009JAMC2286.1, 2010.
- 679 Bedka, K. M.: Overshooting cloud top detections using MSG SEVIRI Infrared brightness
680 temperatures and their relationship to severe weather over Europe, *Atmos. Res.*, 99(2), 175–189,
681 doi:10.1016/j.atmosres.2010.10.001, 2011.
- 682 Bedka, K. M. and Khlopenkov, K.: A probabilistic multispectral pattern recognition method for
683 detection of overshooting cloud tops using passive satellite imager observations, *J. Appl.*
684 *Meteorol. Climatol.*, 55(9), 1983–2005, doi:10.1175/JAMC-D-15-0249.1, 2016.
- 685 Bedka, K. M., Allen, J. T., Punge, H. J., Kunz, M. and Simanovic, D.: A long-term overshooting
686 convective cloud-top detection database over Australia derived from MTSAT Japanese
687 Advanced Meteorological Imager Observations, *J. Appl. Meteorol. Climatol.*, 57(4), 937–951,
688 doi:10.1175/JAMC-D-17-0056.1, 2018.
- 689 Bosilovich, M. G., Lucchesi, R. and Suarez, M.: MERRA-2: File Specification, *Earth*, 9(9), 73
690 [online] Available from: http://gmao.gsfc.nasa.gov/pubs/office_notes/, 2016.
- 691 Chung, E. S., Sohn, B. J., Schmetz, J. and Koenig, M.: Diurnal variation of upper tropospheric
692 humidity and its relations to convective activities over tropical Africa, *Atmos. Chem. Phys.*,
693 2489–2502, doi:www.atmos-chem-phys.net/7/2489/2007/, 2007.
- 694 Chung, E. S., Sohn, B. J. and Schmetz, J.: CloudSat shedding new light on high-reaching tropical
695 deep convection observed with Meteosat, *Geophys. Res. Lett.*, 35(2), 1–5,
696 doi:10.1029/2007GL032516, 2008.
- 697 Dworak, R., Bedka, K., Brunner, J. and Feltz, W.: Comparison between GOES-12 overshooting-
698 top detections, WSR-88D radar reflectivity, and severe storm reports, *Weather Forecast.*, 27(3),
699 684–699, doi:10.1175/WAF-D-11-00070.1, 2012.
- 700 Funk, C., Verdin, A., Michaelsen, J., Peterson, P., Pedreros, D. and Husak, G.: A global satellite-
701 assisted precipitation climatology, *Earth Syst. Sci. Data*, 7(2), 275–287, doi:10.5194/essd-7-275-
702 2015, 2015.
- 703 Geerts, B., Giangrande, S. E., McFarquhar, G. M., Xue, L., Abel, S. J., Comstock, J. M.,
704 Crewell, S., DeMott, P. J., Ebell, K., Field, P., Hill, T. C. J., Hunzinger, A., Jensen, M. P.,
705 Johnson, K. L., Juliano, T. W., Kollias, P., Kosovic, B., Lackner, C., Luke, E., Lüpkes, C.,
706 Matthews, A. A., Neggers, R., Ovchinnikov, M., Powers, H., Shupe, M. D., Spengler, T.,
707 Swanson, B. E., Tjernström, M., Theisen, A. K., Wales, N. A., Wang, Y., Wendisch, M. and Wu,
708 P.: The COMBLE Campaign: A Study of Marine Boundary Layer Clouds in Arctic Cold-Air
709 Outbreaks, *Bull. Am. Meteorol. Soc.*, 103(5), E1371–E1389, doi:10.1175/bams-d-21-0044.1,
710 2022.
- 711 Gettelman, A., Salby, M. L. and Sassi, F.: Distribution and influence of convection in the



- 712 tropical tropopause region, *J. Geophys. Res. Atmos.*, 107(9–10), doi:10.1029/2001jd001048,
713 2002.
- 714 Gettelman, A., Forster, P. M. de F., Fujiwara, M., Fu, Q., Voïmel, H., Gohar, L. K., Johanson,
715 C. and Ammerman, M.: Radiation balance of the tropical tropopause layer, *J. Geophys. Res.*,
716 109(D7), D07103, doi:10.1029/2003JD004190, 2004.
- 717 Griffin, S. M.: Climatology of tropical overshooting tops in North Atlantic tropical cyclones, *J.*
718 *Appl. Meteorol. Climatol.*, 56(6), 1783–1796, doi:10.1175/JAMC-D-16-0413.1, 2017.
- 719 Griffin, S. M., Bedka, K. M. and Velden, C. S.: A method for calculating the height of
720 overshooting convective cloud tops using satellite-based IR imager and CloudSat cloud profiling
721 radar observations, *J. Appl. Meteorol. Climatol.*, 55(2), 479–491, doi:10.1175/JAMC-D-15-
722 0170.1, 2016.
- 723 Grise, K. M., Thompson, D. W. J. and Birner, T.: A global survey of static stability in the
724 stratosphere and upper troposphere, *J. Clim.*, 23, 2275–2292, doi:10.1175/2009JCLI3369.1,
725 2010.
- 726 Groenemeijer, P., Púčik, T., Holzer, A. M., Antonescu, B., Riemann-Campe, K., Schultz, D. M.,
727 Kühne, T., Feuerstein, B., Brooks, H. E., Doswell, C. A., Koppert, H. J. and Sausen, R.: Severe
728 convective storms in Europe: Ten years of research and education at the European Severe Storms
729 Laboratory, *Bull. Am. Meteorol. Soc.*, 98(12), 2641–2651, doi:10.1175/BAMS-D-16-0067.1,
730 2017.
- 731 Heymsfield, G. M., Tian, L., Heymsfield, A. J., Li, L. and Guimond, S.: Characteristics of deep
732 tropical and subtropical convection from nadir-viewing high-altitude airborne doppler radar, *J.*
733 *Atmos. Sci.*, 67(2), 285–308, doi:10.1175/2009JAS3132.1, 2010.
- 734 Hong, G., Heygster, G., Miao, J. and Kunzi, K.: Detection of tropical deep convective clouds
735 from AMSU-B water vapor channels measurements, *J. Geophys. Res. D Atmos.*, 110(5), 1–15,
736 doi:10.1029/2004JD004949, 2005.
- 737 Hong, G., Heygster, G., Notholt, J. and Buehler, S. A.: Interannual to diurnal variations in
738 tropical and subtropical deep convective clouds and convective overshooting from seven years of
739 AMSU-B measurements, *J. Clim.*, 21(17), 4168–4189, doi:10.1175/2008JCLI1911.1, 2008.
- 740 Hong, Y. and Di Girolamo, L.: Cloud Phase Characteristics Over Southeast Asia from A-Train
741 Satellite Observations, *Atmos. Chem. Phys.*, (20), 8267–8291, doi:https://doi.org/10.5194/acp-
742 20-8267-2020, 2020.
- 743 Hou, A. Y., Kakar, R. K., Neeck, S., Azarbarzin, A. A., Kummerow, C. D., Kojima, M., Oki, R.,
744 Nakamura, K. and Iguchi, T.: The global precipitation measurement mission, *Bull. Am.*
745 *Meteorol. Soc.*, 95(5), 701–722, doi:10.1175/BAMS-D-13-00164.1, 2014.
- 746 Hourngir, D., Panegrossi, G., Casella, D., Sanò, P., D’adderio, L. P. and Liu, C.: A 4-year
747 climatological analysis based on gpm observations of deep convective events in the
748 mediterranean region, *Remote Sens.*, 13(9), 1–21, doi:10.3390/rs13091685, 2021.
- 749 Iguchi, T., R. Meneghini, 2021: GPM DPR Precipitation Profile L2A 1.5 hours 5 km V07,
750 Greenbelt, MD, Goddard Earth Sciences Data and Information Services Center (GES DISC),
751 Accessed: 14 March 2020, 10.5067/GPM/DPR/GPM/2A/07.



- 752 Janiga, M. A. and Thorncroft, C. D.: Convection over tropical Africa and the East Atlantic
753 during the West African monsoon: Regional and diurnal variability, *J. Clim.*, 27(11), 4189–4208,
754 doi:10.1175/JCLI-D-13-00449.1, 2014.
- 755 Jeyaratnam, J., Luo, Z. J., Giangrande, S. E., Wang, D. and Masunaga, H.: A Satellite-Based
756 Estimate of Convective Vertical Velocity and Convective Mass Flux: Global Survey and
757 Comparison With Radar Wind Profiler Observations, *Geophys. Res. Lett.*, 48(1), 1–11,
758 doi:10.1029/2020GL090675, 2021.
- 759 Johnson, R. H.: Diurnal cycle of monsoon convection, in *The global monsoon system: Research*
760 *and forecast*, pp. 257–276, Singapore: World Scientific., 2011.
- 761 Khlopenkov, K. V., Bedka, K. M., Cooney, J. W. and Iitterly, K.: Recent Advances in Detection
762 of Overshooting Cloud Tops From Longwave Infrared Satellite Imagery, *J. Geophys. Res.*
763 *Atmos.*, 126(14), 1–25, doi:10.1029/2020jd034359, 2021.
- 764 King, M. D., Kaufman, Y. J., Menzel, W. P. and Tanré, D.: Remote sensing of cloud, aerosol,
765 and water vapor properties from the Moderate Resolution Imaging Spectrometer (MODIS), *IEEE*
766 *Trans. Geosci. Remote Sens.*, 30, 2–27, doi:10.1109/36.124212, 1992.
- 767 LAADS DAAC: Level-1 Atmosphere Archive & Distribution Sys- tem Distributed Active
768 Archive Center for MODIS data, avail- able at: <https://ladsweb.modaps.eosdis.nasa.gov/>, last
769 access: 10 March 2022.
- 770 Li, H., Wei, X., Min, M., Li, B., Nong, Z. and Chen, L.: A Dataset of Overshooting Cloud Top
771 from 12-Year CloudSat/CALIOP Joint Observations, *Remote Sens.*, 14(10), 2417,
772 doi:10.3390/rs14102417, 2022.
- 773 Liu, C. and Zipser, E. J.: Global distribution of convection penetrating the tropical tropopause, *J.*
774 *Geophys. Res. Atmos.*, 110(23), 1–12, doi:10.1029/2005JD006063, 2005.
- 775 Liu, N. and Liu, C.: Global distribution of deep convection reaching tropopause in 1 year GPM
776 observations, *NJournal Geophys. Res. Atmospheres*, 121, 3924–3842, doi:10.1002/
777 2015JD024430, 2016.
- 778 Liu, N., Liu, C. and Hayden, L.: Climatology and Detection of Overshooting Convection From
779 4 Years of GPM Precipitation Radar and Passive Microwave Observations, *J. Geophys. Res.*
780 *Atmos.*, 125(7), 1–14, doi:10.1029/2019JD032003, 2020.
- 781 Marchand, R., Mace, G. G., Ackerman, T. and Stephens, G.: Hydrometeor detection using
782 Cloudsat - An earth-orbiting 94-GHz cloud radar, *J. Atmos. Ocean. Technol.*, 25(4), 519–533,
783 doi:10.1175/2007JTECHA1006.1, 2008.
- 784 Marion, G. R., Trapp, R. J. and Nesbitt, S. W.: Using overshooting top area to discriminate
785 potential for large, intense tornadoes, *Geophys. Res. Lett.*, 46(21), 12520–12526,
786 doi:10.1029/2019GL084099, 2019.
- 787 Monette, S. A., Velden, C. S., Griffin, K. S. and Rozoff, C. M.: Examining trends in satellite-
788 detected tropical overshooting tops as a potential predictor of tropical cyclone rapid
789 intensification, *J. Appl. Meteorol. Climatol.*, 51(11), 1917–1930, doi:10.1175/JAMC-D-11-
790 0230.1, 2012.



- 791 Murphy, A. M., Rauber, R. M., McFarquhar, G. M., Finlon, J. A., Plummer, D. M., Rosenow, A.
792 A. and Jewett, B. F.: A microphysical analysis of elevated convection in the comma head region
793 of continental winter cyclones, *J. Atmos. Sci.*, 74(1), 69–91, doi:10.1175/JAS-D-16-0204.1,
794 2017.
- 795 Nesbitt, S. W. and Zipser, E. J.: The diurnal cycle of rainfall and convective intensity according
796 to three years of TRMM measurements, *J. Clim.*, 16, 1456–1475, doi:10.1175/1520-0442-
797 16.10.1456, 2003.
- 798 Papritz, L., Rouges, E., Aemisegger, F. and Wernli, H.: On the Thermodynamic Preconditioning
799 of Arctic Air Masses and the Role of Tropopause Polar Vortices for Cold Air Outbreaks From
800 Fram Strait, *J. Geophys. Res. Atmos.*, 124(21), 11033–11050, doi:10.1029/2019JD030570, 2019.
- 801 Partain, P.: Cloudsat ECMWF-AUX auxiliary data process description and interface control
802 document, Coop. Inst. Res. Atmos. Color. State Univ. [online] Available from:
803 http://129.82.109.192/ICD/ECMWF-AUX/ECMWF-AUX_PDICD_3.0.pdf, 2007.
- 804 Platnick, S., King, M. D., Ackerman, S. A., Menzel, W. P., Baum, B. A., Riédi, J. C. and Frey,
805 R. A.: The MODIS cloud products : Algorithms and examples from Terra, *IEEE Trans. Geosci.*
806 *Remote Sens.*, 41, 459–473, doi:10.1109/TGRS.2002.808301, 2003.
- 807 Proud, S. R.: Analysis of overshooting top detections by Meteosat Second Generation: A 5-year
808 dataset, *Q. J. R. Meteorol. Soc.*, 141(688), 909–915, doi:10.1002/qj.2410, 2015.
- 809 Rauber, R. M., Wegman, J., Plummer, D. M., Rosenow, A. A., Peterson, M., McFarquhar, G.
810 M., Jewett, B. F., Leon, D., Market, P. S., Knupp, K. R., Keeler, J. M. and Battaglia, S. M.:
811 Stability and charging characteristics of the comma head region of continental winter cyclones, *J.*
812 *Atmos. Sci.*, 71(5), 1559–1582, doi:10.1175/JAS-D-13-0253.1, 2014.
- 813 Rauber, R. M., Plummer, D. M., Macomber, M. K., Rosenow, A. A., McFarquhar, G. M., Jewett,
814 B. F., Leon, D., Owens, N. and Keeler, J. M.: The role of cloud-top generating cells and
815 boundary layer circulations in the finescale radar structure of a winter cyclone over the great
816 lakes, *Mon. Weather Rev.*, 143(6), 2291–2318, doi:10.1175/MWR-D-14-00350.1, 2015.
- 817 Rysman, J. F., Claud, C. and Delanoe, J.: Monitoring Deep Convection and Convective
818 Overshooting from 60° S to 60° N Using MHS: A Cloudsat/CALIPSO-Based Assessment, *IEEE*
819 *Geosci. Remote Sens. Lett.*, 14(2), 159–163, doi:10.1109/LGRS.2016.2631725, 2017.
- 820 Schmetz, J., Tjemkes, S. A., Gube, M. and Van De Berg, L.: Monitoring deep convection and
821 convective overshooting with METEOSAT, *Adv. Sp. Res.*, 19(3), 433–441, doi:10.1016/S0273-
822 1177(97)00051-3, 1997.
- 823 Setvák, M., Rabin, R. M. and Wang, P. K.: Contribution of the MODIS instrument to
824 observations of deep convective storms and stratospheric moisture detection in GOES and MSG
825 imagery, *Atmos. Res.*, 83(2-4 SPEC. ISS.), 505–518, doi:10.1016/j.atmosres.2005.09.015, 2007.
- 826 Setvák, M., Bedka, K., Lindsey, D. T., Sokol, A., Charvát, Z., Šťástka, J. and Wang, P. K.: A-
827 Train observations of deep convective storm tops, *Atmos. Res.*, 123, 229–248,
828 doi:10.1016/j.atmosres.2012.06.020, 2013.
- 829 Shikhov, A., Chernokulsky, A., Kalinin, N., Bykov, A. and Pischalnikova, E.: Climatology and
830 Formation Environments of Severe Convective Windstorms and Tornadoes in the Perm Region



831 (Russia) in 1984-2020, *Atmosphere (Basel)*, (12), 1407, doi:<https://doi.org/10.3390/atmos12111407>, 2021.

832

833 Stephens, G. L., Vane, D. G., Boain, R. J., Mace, G. G., Sassen, K., Wang, Z., Illingworth, A. J.,
834 O'Connor, E. J., Rossow, W. B., Durden, S. L., Miller, S. D., Austin, R. T., Benedetti, A. and
835 Mitrescu, C.: The cloudsat mission and the A-Train: A new dimension of space-based
836 observations of clouds and precipitation, *Bull. Am. Meteorol. Soc.*, 83, 1771–1790,
837 doi:10.1175/BAMS-83-12-1771, 2002.

838 Stephens, G. L., Vane, D. G., Tanelli, S., Im, E., Durden, S., Rokey, M., Reinke, D., Partain, P.,
839 Mace, G. G., Austin, R., L'Ecuyer, T., Haynes, J., Lebsock, M., Suzuki, K., Waliser, D., Wu, D.,
840 Kay, J., Gettelman, A., Wang, Z. and Marchand, R.: CloudSat mission: Performance and early
841 science after the first year of operation, *J. Geophys. Res.*, 113, D00A18,
842 doi:10.1029/2008JD009982, 2008.

843 Stewart, R. E., Szeto, K. K., Reinking, R. F., Clough, S. A. and Ballard, S. P.: Midlatitude
844 cyclonic cloud systems and their features affecting large scales and climate, *Rev. Geophys.*,
845 36(2), 245–273, doi:10.1029/97RG03573, 1998.

846 Sun, L. X., Zhuge, X. Y. and Wang, Y.: A Contour-Based Algorithm for Automated Detection of
847 Overshooting Tops Using Satellite Infrared Imagery, *IEEE Trans. Geosci. Remote Sens.*, 57(1),
848 497–508, doi:10.1109/TGRS.2018.2857486, 2019.

849 Tao, C. and Jiang, H.: Global distribution of hot towers in tropical cyclones based on 11-Yr
850 TRMM data, *J. Clim.*, 26(4), 1371–1386, doi:10.1175/JCLI-D-12-00291.1, 2013.

851 Terpstra, A., Renfrew, I. A. and Sergeev, D. E.: Characteristics of cold-air outbreak events and
852 associated polar mesoscale cyclogenesis over the north Atlantic region, *J. Clim.*, 34(11), 4567–
853 4584, doi:10.1175/JCLI-D-20-0595.1, 2021.

854 Tian, B., Soden, B. J. and Wu, X.: Diurnal cycle of convection, clouds, and water vapor in the
855 tropical upper troposphere: Satellites versus a general circulation model, *J. Geophys. Res. D*
856 *Atmos.*, 109(10), 1–16, doi:10.1029/2003JD004117, 2004.

857 Tian, B., Held, I. M., Lau, N. C. and Soden, B. J.: Diurnal cycle of summertime deep convection
858 over North America: A satellite perspective, *J. Geophys. Res. D Atmos.*, 110(8), 1–10,
859 doi:10.1029/2004JD005275, 2005.

860 Trapp, R. J., Marion, G. R. and Nesbitt, S. W.: The regulation of tornado intensity by updraft
861 width, *J. Atmos. Sci.*, 74(12), 4199–4211, doi:10.1175/JAS-D-16-0331.1, 2017.

862 Wang, C., Luo, Z. J. and Huang, X.: Parallax correction in collocating CloudSat and Moderate
863 Resolution Imaging Spectroradiometer (MODIS) observations: Method and application to
864 convection study, *J. Geophys. Res. Atmos.*, 116(17), 1–9, doi:10.1029/2011JD016097, 2011.

865 Wang, Z., Vane, D. and Staphens, G.: Level 2 Combined Radar and Lidar Cloud Scenario
866 Classification Product Process Description and Interface Control document. [online] Available
867 from:
868 <http://scholar.google.com/scholar?hl=en&btnG=Search&q=intitle:Level+2+Combined+Radar+and+Lidar+Cloud+Scenario+Classification+Product+Process+Description+and+Interface+Control+Document#1>, 2012.
869
870



- 871 Wilcox, L. J., Hoskins, B. J. and Shine, K. P.: A global blended tropopause based on ERA data.
872 Part I: Climatology, *Q. J. R. Meteorol. Soc.*, 138(664), 561–575, doi:10.1002/qj.951, 2012.
- 873 Winker, D. M., Pelon, J. R. and McCormick, M. P.: The CALIPSO mission: Spaceborne lidar for
874 observation of aerosols and clouds, *Lidar Remote Sens. Ind. Environ. Monit.* III, 4893, 1–11,
875 doi:10.1117/12.466539, 2003.
- 876 Xiong, X., Sun, J., Wu, A., Chiang, K.-F., Esposito, J. and Barnes, W.: Terra and Aqua MODIS
877 calibration algorithms and uncertainty analysis, *Sensors, Syst. Next-Generation Satell.* IX,
878 5978(November 2015), 59780V, doi:10.1117/12.627631, 2005.
- 879 Xiong, X., Angal, A., Barnes, W. L., Chen, H., Chiang, V., Geng, X., Li, Y., Twedt, K., Wang,
880 Z., Wilson, T. and Wu, A.: Updates of Moderate Resolution Imaging Spectroradiometer on-orbit
881 calibration uncertainty assessments, *J. Appl. Remote Sens.*, 12(03), 1,
882 doi:10.1117/1.jrs.12.034001, 2018.
- 883 Yuter, S. E. and Houze, R. A.: Three-dimensional kinematic and microphysical evolution of
884 Florida cumulonimbus. Part II: Frequency distributions of vertical velocity, reflectivity, and
885 differential reflectivity, *Mon. Weather Rev.*, 123, doi:https://doi.org/10.1175/1520-
886 0493(1995)123<1941:TDKAME>2.0.CO;2, 1995.
- 887 Zhuge, X. Y., Ming, J. and Wang, Y.: Reassessing the use of inner-core hot towers to predict
888 tropical cyclone rapid intensification, *Weather Forecast.*, 30(5), 1265–1279, doi:10.1175/WAF-
889 D-15-0024.1, 2015.
- 890 Zipser, E. J., Cecil, D. J., Liu, C., Nesbitt, S. W. and Yorty, D. P.: Where are the most intense
891 thunderstorms on Earth?, *Bull. Am. Meteorol. Soc.*, 87(8), 1057–1071, doi:10.1175/BAMS-87-
892 8-1057, 2006.
- 893